Geology
GSA Data Repository 2019049

Widespread seismic anisotropy in Earth's lowermost mantle beneath the Atlantic and Siberia

DOI:10.1130/G45514.1

Michael Grund, Joachim R. R. Ritter
(Email: michael.grund@kit.edu)

Karlsruhe Institute of Technology (KIT), Geophysical Institute, Karlsruhe, Germany

Correction of sensor misalignments

Possible sensor misalignments were checked by comparing the initial and corrected particle motions of the RC and SC methods. Differences in the results can hint towards a possible misalignment of the horizontal components of the sensor (e.g. Tian et al., 2011; Lynner & Long, 2012). Finally, we oriented each station such that the linear particle motions of the individual events are parallel to their corresponding backazimuth directions (Lynner & Long, 2012). Individual sensor misalignments, if detected, are reported in our previous work (Grund et al., 2017) and in Table DR1.

Figures and tables

• **Table DR1** (***Table_DR1_Grund_Ritter_2018.xlsx***, file uploaded separately) contains all SKS-SKKS shear wave splitting (ϕ and δt) and splitting intensity (SI) measurements conducted for this study along with their uncertainties (95% confidence interval) and information about stations and events. Additionally the SKS-SKKS core-mantle boundary (CMB) pierce points (red-orange and white-white circles in the maps shown in this study) calculated with the tauP toolkit (Crotwell et al., 1999) and the iasp91 earth model (Kennett, 1991) are provided (e.g. for reproduction in other studies). The last three columns list the detected sensor misalignments for the corresponding stations as well as the low and high corner frequencies of the filter used for the individual phases. Although the corners were partly slightly adjusted (see main text), for each single SKS-SKKS pair the same configuration was used to ensure consistency between the two phases.

• **Figure DR2** shows stereoplots for two exemplary long-running permanent stations at which a strong backazimuthal variation for ϕ and δt is observed. Note the relatively simple pattern observed for phase arrivals of South American earthquakes (SKS mostly null, SKKS clearly split). In

contrast for the eastern direction (earthquake sources beneath Tonga/Fiji and Vanuatu/Indonesia) the splitting pattern is much more complex.

• **Figure DR3** displays further high-quality discrepant SKS-SKKS waveform examples.

• **Figure DR4** shows the raypaths of SKS, SKKS and sSKS. In comparison to SKS the raypath for sSKS contains an additional leg that results from a reflection of an upgoing shear wave at the free surface. High quality SKS, SKKS and sSKS waveform examples of one event in 2016, observed at several stations across the network, are shown as well. sSKKS phases could not be observed in our records with a sufficiently high enough SNR.

• **Figure DR5** shows the Fresnel zone estimates of the 49 discrepant SKS-SKKS pairs for a dominant period of 8 s following Favier & Chevrot (2003) in four different depths (120 km, 210 km, 410 km and 510 km). The centers of the Fresnel zones correspond to the pierce points calculated with the tauP toolkit (Crotwell et al., 1999) and the iasp91 earth model (Kennett, 1991). It is obvious that for both phases the Fresnel zones overlap significantly down to the depth of the mantle transition zone. Thus we conclude that lowermost mantle anisotropy contributes to the overall splitting signal, since otherwise the same characteristics would be expected for both phases.

• **Figure DR6** shows the distribution of SKS-SKKS pairs over the epicentral distance measured between the event and the receiver and over the event depth. The pairs are categorized based on their observed splitting characteristics (yellow and green: one phase split the other null, blue: both phases split, purple: both phases null).

• **Figure DR7** and **Figure DR8** display exemplary record sections with seismograms of the radial and transverse components of events below Papua New Guinea (2016/08/31, arrivals from east) and below Chile (2016/07/25, arrivals from west). The different phase arrivals (SKS, SKKS, Sdiff, sSKS etc.) in both record sections are well separated and thus we assume no major wave interference between different phases that could explain the observed SKS-SKKS discrepancies without a contribution from anisotropy in the lowermost mantle.

• **Figure DR9** shows the individual shear wave splitting results atop the GyPSuM model (Simmons et al., 2010) in 2700 km depth. Besides the discrepant pairs also the non-discrepant pairs with both phases split are shown. For the eastern region several split-split pairs are observed which are often located in regions where also clear discrepancies appear. Geographically the patterns in general are consistent within the different areas and therefore we cannot rule out that for the split-split cases, SKS and SKKS are affected by lowermost mantle anisotropy in the same way (as mentioned in the main text). However, in contrast we also cannot separate the likely deep contributions from more shallower ones due to the partly complex pattern at the recording stations

(see Fig. DR2).

• **Figure DR10** displays the D" pierce points of the discrepant SKS-SKKS pairs along with the measured ΔSI values (difference in splitting intensity).

• **Figure DR11** displays the locations of the stations shown in Figures DR7 and DR8 atop the simplified geological units of Scandinavia after Gaál & Gorbatschev (1987); Gorbatchev (2004) as well as the raypaths for the two events below Papua New Guinea on 2016/08/31 and Chile on 2016/07/25. Since similar pattern for the split phases are seen across different geological terranes (see main text), a large scale feature of deep anisotropy is assumed to be responsible for the observations.

• **Figure DR12** shows the individual shear wave splitting results (see Fig. 3 in main text) atop the results of the vote map analysis for several global tomography models of Shepard et al. (2017) in 2,700 km depth. High votes denote areas of robust fast velocity structures (possibly related to remnants of subducted slabs) based on seven global shear wave tomography models (including GyPSuM). The high vote below Siberia indicates that the fast anomaly visible in Fig. 3 (see main text) is a robust feature that is likely related to material of an old subducted slab (Van der Voo et al., 1999).

• **Figure DR13** shows the individual shear wave splitting results atop the results of the cluster analysis of Lekic et al. (2012). High votes denote areas of robust slow velocity structures in the lower mantle based on five global shear wave tomography models (including GyPSuM).

• **Figure DR14** shows an overview about areas in which anomalous lower- most mantle structure was observed based on different seismic phase types.

Data information and availability

• For two permanent stations (LVZ and VSU) that were previously studied in the context of lowermost mantle anisotropy (Fig. DR14, Long & Lynner, 2015), we continued the analysis with more recent recordings (2012-2017).
• The data set that was used to generate the fast anomaly vote map (Shepard et al., 2017) in Fig. DR12 is freely accessible here: `http://folk.uio.no/gracees/Shephard_SlabVoteMaps` (last accessed: 11 January 2018). The data grid to create the cluster analysis (Lekic et al., 2012) shown in Fig. DR13 can be downloaded from: `https://www.geol.umd.edu/facilities/seismology/data/clustering-of-lower-mantle-structure-perm-anomaly/` (last accessed: 21 December 2017)

References

Crotwell, H. P., Owens, T. J., & Ritsema, J., 1999. The TauP toolkit: Flexible seismic travel-time and ray-path utilities, *Seismol. Res. Lett.*, **70**, 154–160.

Favier, N. & Chevrot, S., 2003. Sensitivity kernels for shear wave splitting in transverse isotropic media, *Geophys. J. Int.*, **153**, 213–228.

Gaál, G. & Gorbatschev, R., 1987. An outline of the Precambrian evolution of the Baltic Shield, *Precambrian Res.*, **35**, 15–52.

Gorbatchev, R., 2004. The Transscandinavian Igneous Belt – introduction and background, in *The Transscandinavian Igneous Belt (TIB) in Sweden: a Review of Its Character and Evolution. Geological Survey of Finland, Special Paper*, vol. 37, pp. 9–15, eds Högdahl, K., Andersson, U., & Eklund, O., Geological Survey of Finland.

Grund, M., Mauerberger, A., Ritter, J. R. R., & Tilmann, F., 2017. Broadband Recordings for LITHOS-CAPP: LITHOspheric Structure of Caledonian, Archaean and Proterozoic Provinces Sep. 2014 - Oct. 2016, Sweden and Finland, (Scientific Technical Report STR-Data 17/02), (GIPP Experiment and Data Archive), Potsdam: GFZ German Research Centre for Geosciences, doi: 10.2312/GFZ.b103-17029.

He, Y., Wen, L., Capdeville, Y., & Zhao, L., 2015. Seismic evidence for an Iceland thermo-chemical plume in the Earth's lowermost mantle, *Earth Planet. Sci. Lett.*, **417**, 19–27.

Helmberger, D. V., Wen, L., & Ding, X., 1998. Seismic evidence that the source of the Iceland hotspot lies at the core-mantle boundary, *Nature*, **396**, 251–255.

Kennett, B. L. N., 1991. IASPEI 1991 seismological tables, *Terra Nova*, **3(2)**, 122.

Lekic, V., Cottaar, S., Dziewonski, A., & Romanowicz, B., 2012. Cluster analysis of global lower mantle tomography: A new class of structure and implications for chemical heterogeneity, *Earth Planet. Sci. Lett.*, **357-358**, 68–77.

Long, M. D. & Lynner, C., 2015. Seismic anisotropy in the lowermost mantle near the Perm Anomaly, *Geophys. Res. Lett.*, **42**, doi:10.1002/2015GL065506.

Lynner, C. & Long, M. D., 2012. Evaluating contributions to SK(K)S splitting from lower mantle anisotropy: A case study from station DBIC, Côte D'Ivoire, *Bull. Seismol. Soc. Am.*, **102(3)**, 1030–1040.

Shepard, G. E., Matthews, K. J., Hosseini, K., & Domeier, M., 2017. On the consistency of seismically imaged lower mantle slabs, *Sci. Rep.*, **7**, 10976.

Silver, P. G. & Chan, W. W., 1991. Shear wave splitting and subcontinental mantle deformation, *J. Geophys. Res*, **96**, 16429–16454.

Simmons, N. A., Forte, A., Boschi, L., & Grand, S., 2010. GyPSuM: A joint tomographic model of mantle density and seismic wave speeds, *Geophys. Res. Lett.*, **115**, B12310, doi:10.1029/2010JB007631.

Thomas, C. & Kendall, J.-M., 2002. The lowermost mantle beneath northern Asia-II. Evidence for lower-mantle anisotropy, *Geophys. J. Int.*, **151**, 296–308.

Tian, X., Zhang, J., Si, S., Wang, J., Chen, Y., & Zhang, Z., 2011. SKS splitting measurements with horizontal component misalignment, *Geophys. J. Int.*, **185**, 329–340.

Van der Voo, R., Spakman, W., & Bijwaard, H., 1999. Mesozoic subducted slabs under Siberia, *Nature*, **397**, 246–249.

Weber, M., 1993. P- and S-wave reflections from anomalies in the lowermost mantle, *Geophys. J. Int.*, **115**, 183–210.

Wookey, J. & Kendall, J.-M., 2008. Constraints on lowermost mantle mineralogy and fabric beneath Siberia from seismic anisotropy, *Earth Planet. Sci. Lett.*, **275**, 32–42.

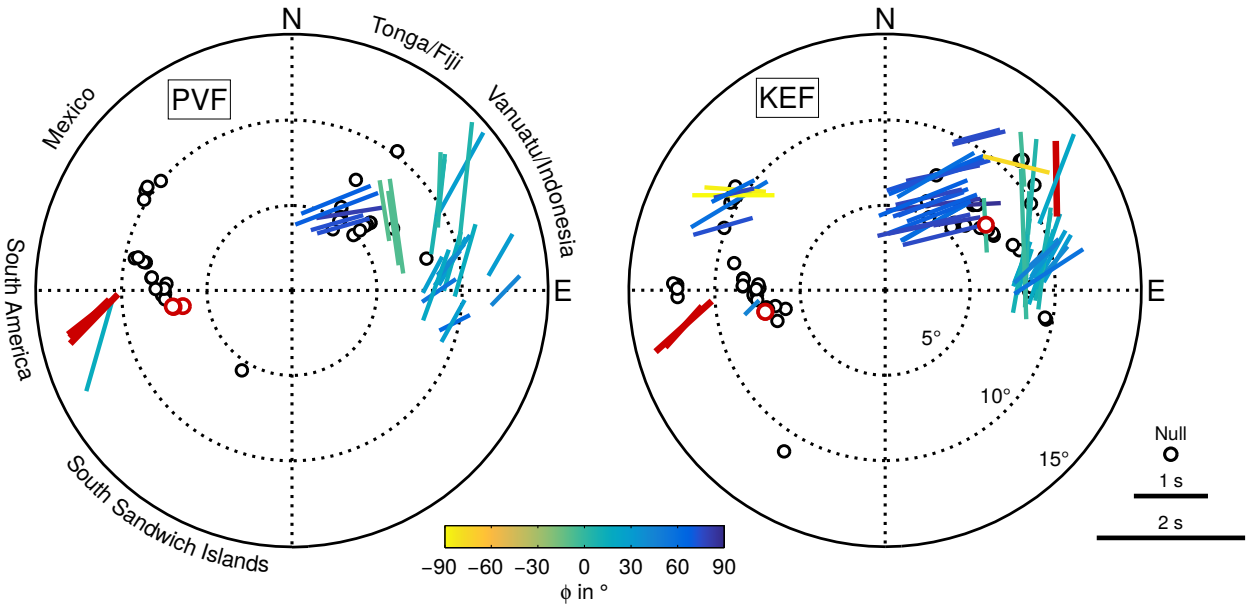

Figure DR2: Exemplary stereoplots for the two long-running permanent stations PVF and KEF at which a strong backazimuthal variation for ϕ and δt is observed. Splitting parameters are shown as a function of backazimuth (clockwise direction from north) and incidence angle (radial axis, 5°-15°). To highlight variations of ϕ with backazimuth the single bars are also color-coded. Black open circles represent null measurements. Discrepant pairs are shown in red.

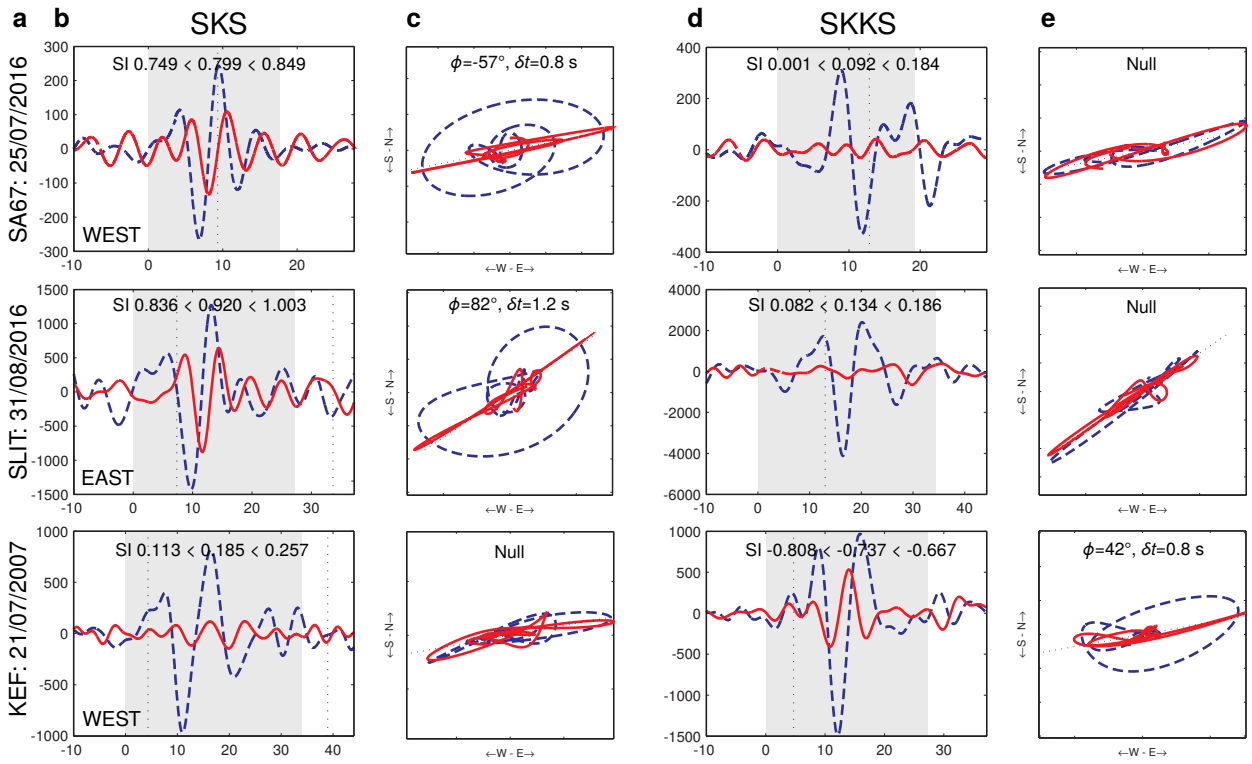

Figure DR3: (a) station and earthquake information for anomalous SKS-SKKS waveforms. (b) original (uncorrected) radial (blue dashed) and transverse (solid red) component seismograms for the SKS phase. At the top the corresponding SI value along with its uncertainty (95% confidence interval) is shown and at the bottom the direction from which the wave arrived (east or west). (c) corresponding particle motions in the horizontal plane before (blue dashed) and after (solid red) correcting the splitting using the SC method Silver & Chan (1991). Splitting parameters ϕ and δt or nulls are indicated at the top of each panel. (d) and (e) corresponding content for the SKKS phase of the same event.

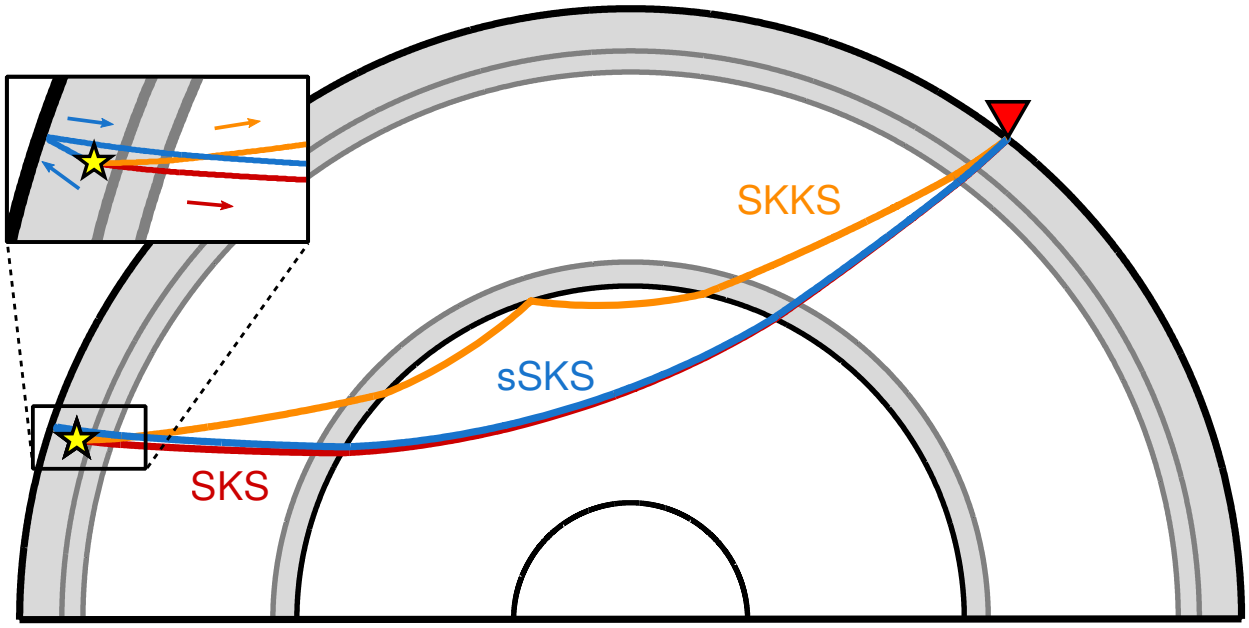

Figure DR4: Raypaths of SKS, SKKS and sSKS from hypocenter (star) to receiver (500 km depth, $\Delta \sim 100°$). In comparison to SKS the raypath for sSKS contains an additional leg that results from a reflection of an upgoing shear wave at the free surface (small blue arrow in inset). Since both phases have nearly identical incidence angles (within $\sim 0.3°$) and raypaths, they also sample the same region in D". Therefore, both raypaths lie almost atop each other after the P-to-S conversion at the core-mantle boundary on the receiver side. (*Fig. continued on next page)*

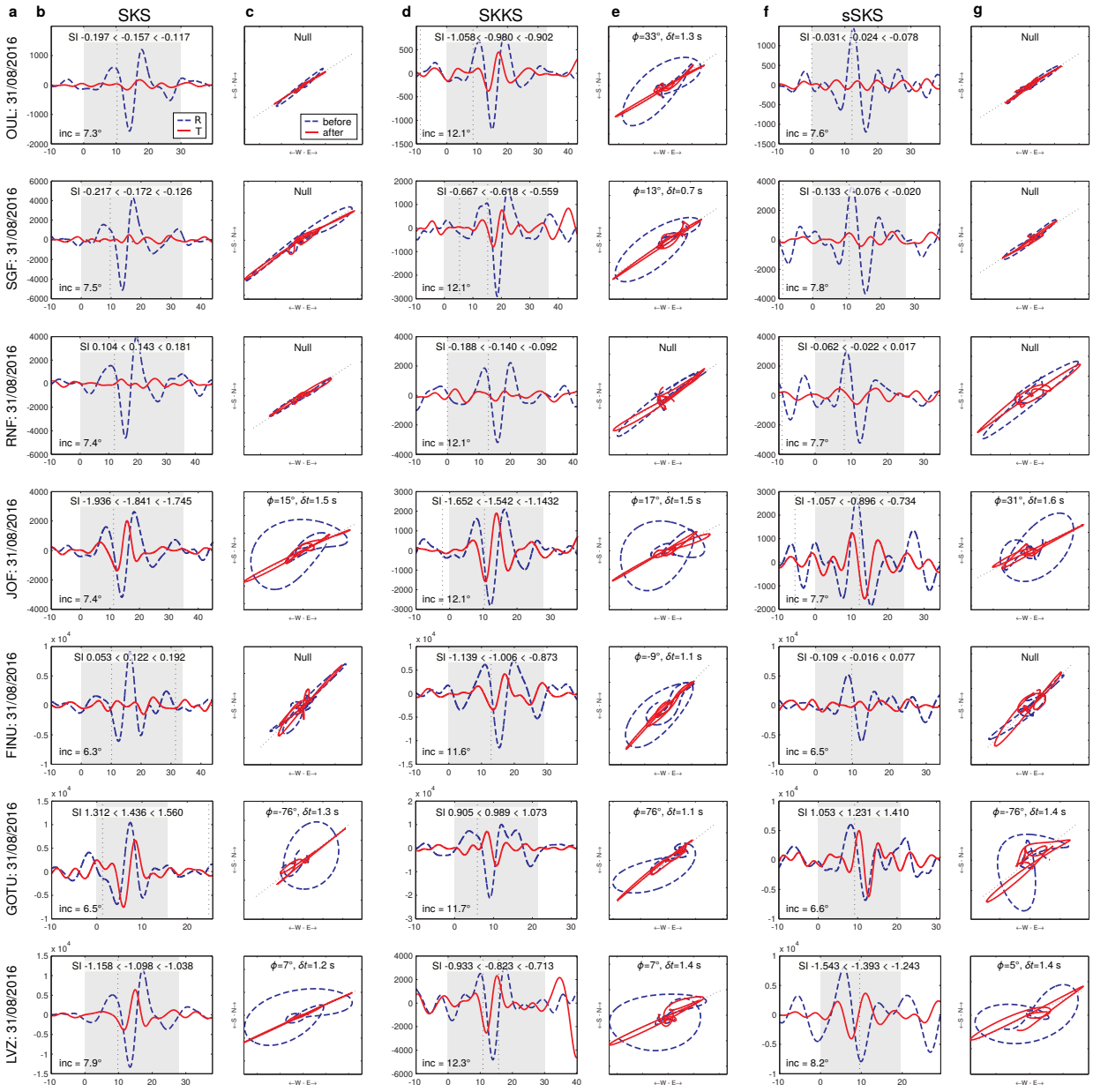

Figure DR4 (Cont.): Waveform examples for SKS, SKKS and sSKS phases. (a) station and event date. (b) original (uncorrected) radial (blue dashed) and transverse (solid red) components for the SKS phase. On top the corresponding SI along with its uncertainty (95% confidence interval) is shown. The incidence angle is given in the lower left corner. The gray shaded area indicates the analysis window. (c) corresponding particle motions before (blue dashed) and after (solid red) the correction for splitting using the SC method Silver & Chan (1991). Splitting parameters or nulls are indicated at the top of each panel. (d) and (e) corresponding content for the SKKS phase of the same event. (f) and (g) corresponding content for the sSKS phase of the same event.

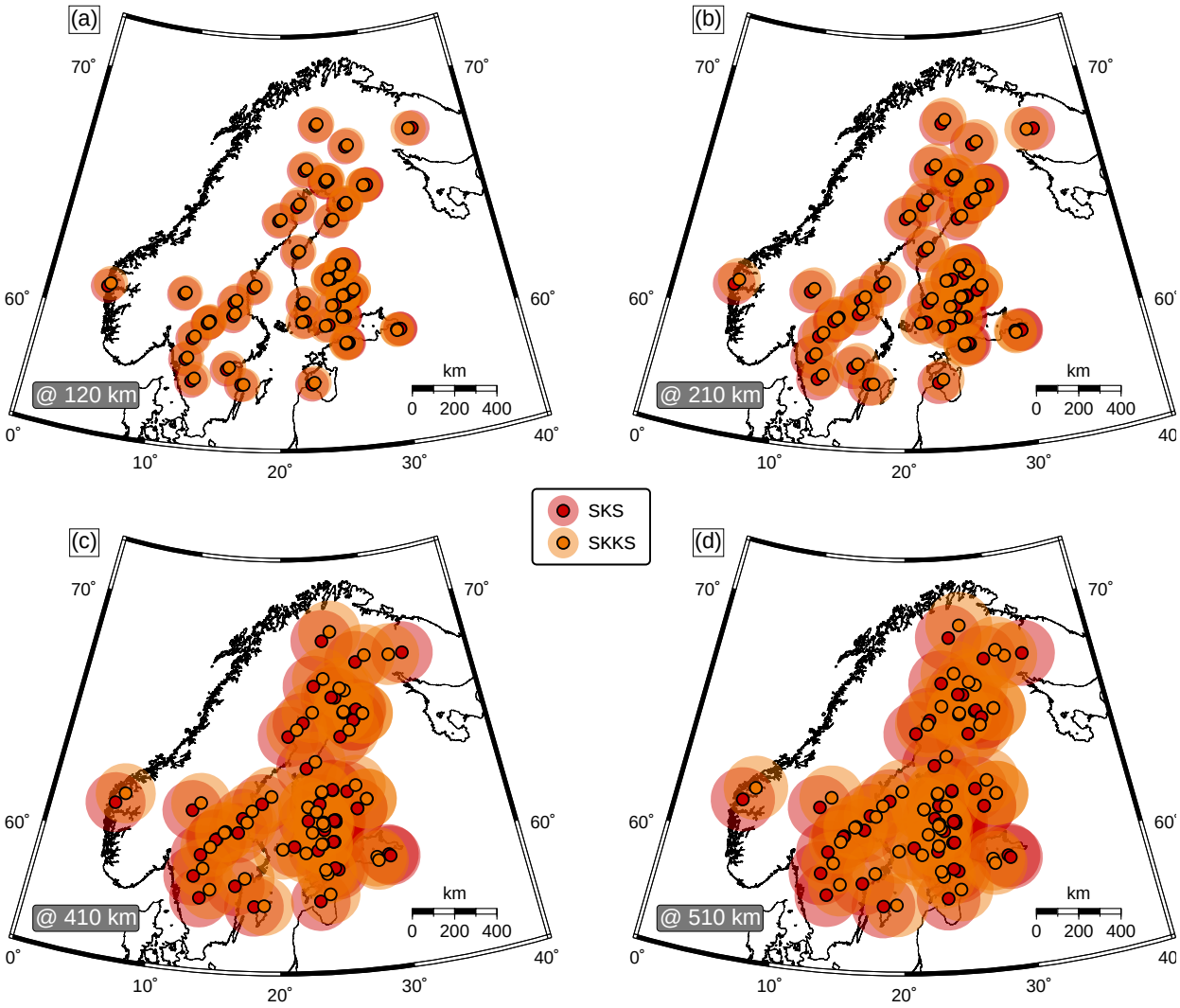

Figure DR5: (a)-(d) Fresnel zone estimates of the 49 discrepant SKS-SKKS pairs (transparent large circles) for a dominant period of 8 s following Favier & Chevrot (2003) in four different depths (120 km, 210 km, 410 km and 510 km). The centers of the Fresnel zones correspond to the pierce points (small black bordered circles) calculated with the tauP toolkit (Crotwell et al., 1999) and the iasp91 earth model (Kennett, 1991)

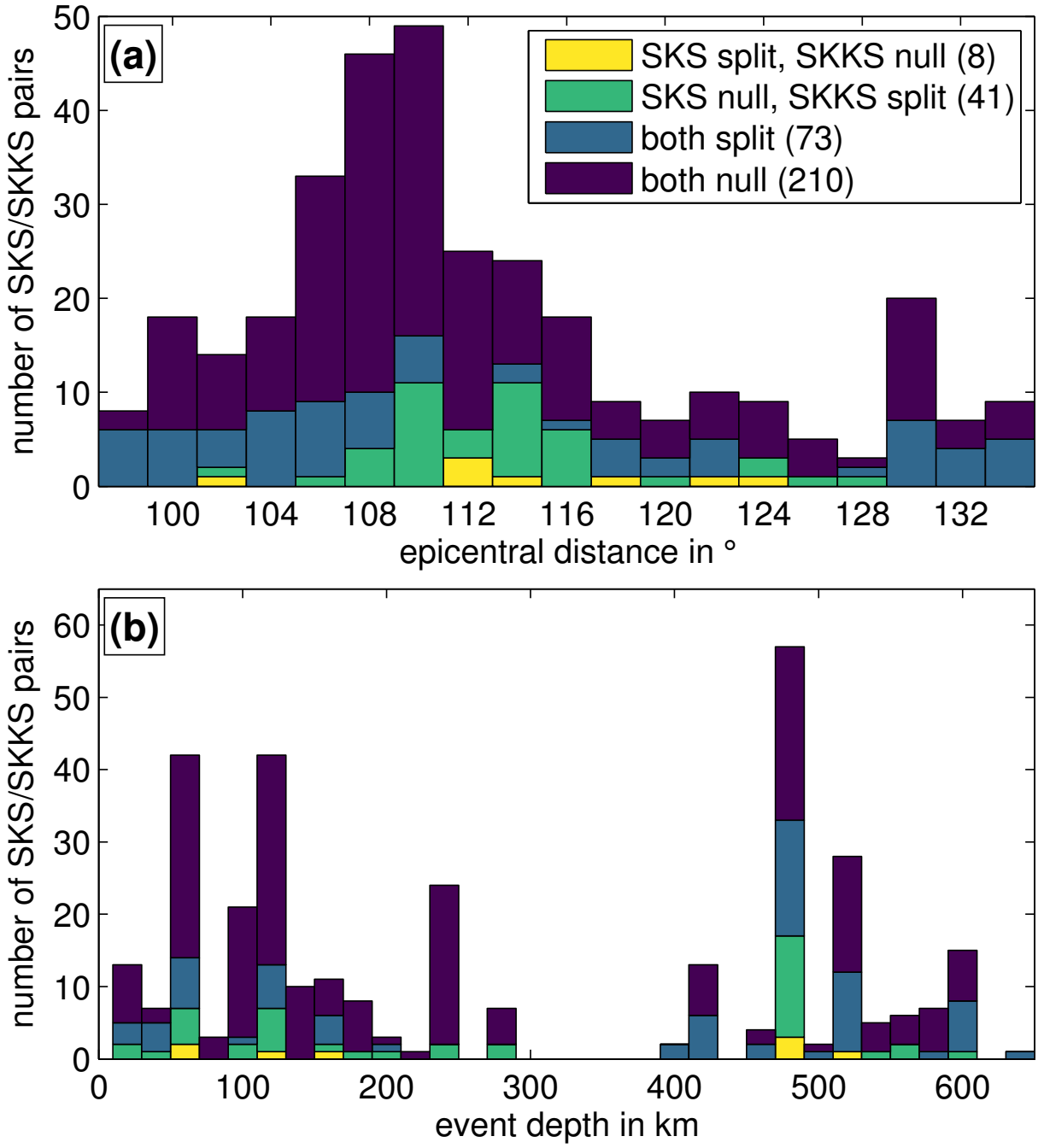

Figure DR6: (a) Distribution of epicentral distances for all SKS-SKKS pairs based on the distance between epicenter and receiver. (b) Distribution of event depths for all SKS-SKKS pairs.

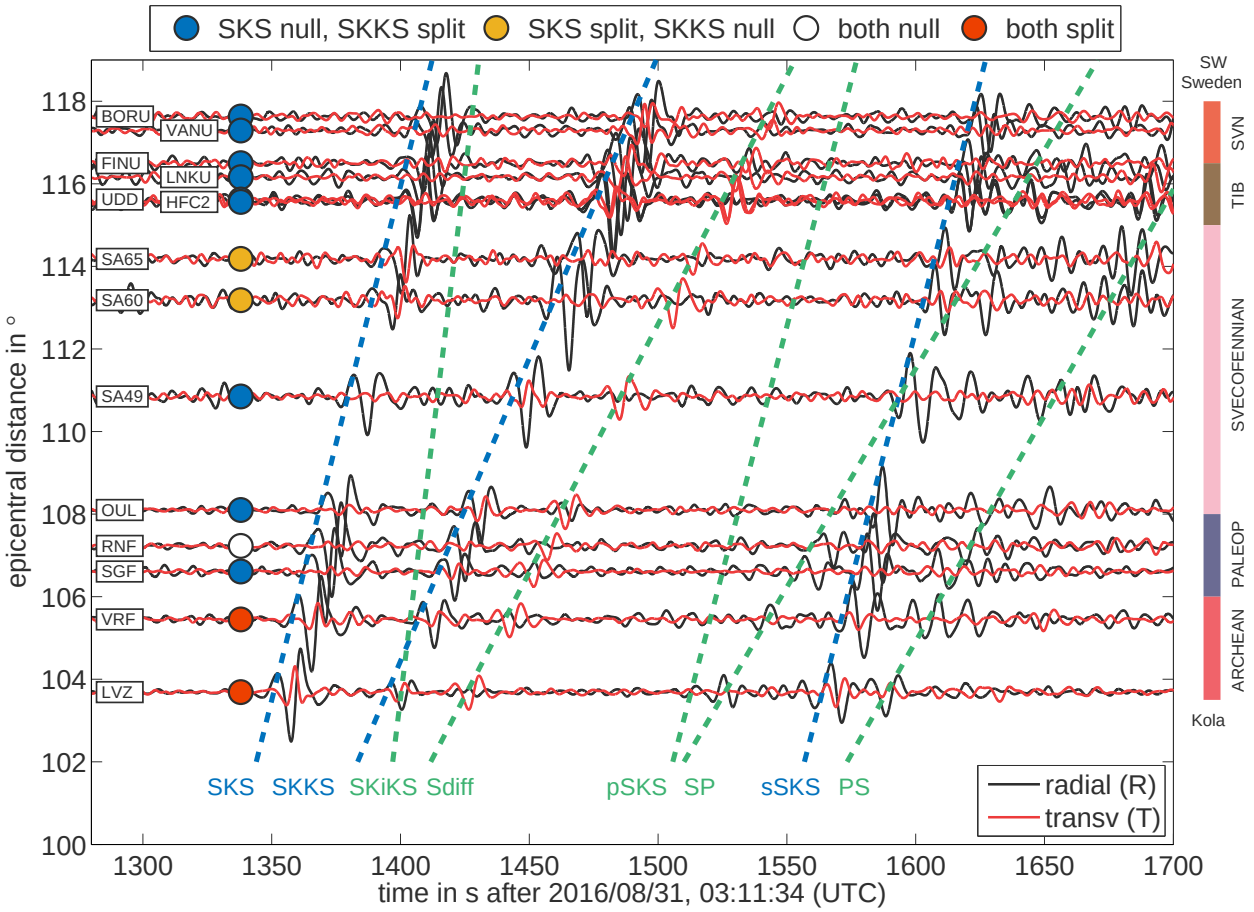

Figure DR7: Record section with seismograms of the radial (black) and transverse (red) components of a Papua New Guinea event on 2016/08/31. Theoretical arrivals of different phases based on the iasp91 earth model (Kennett, 1991) are shown as dashed lines. Blue indicates phases that were used in this study to probe lowermost mantle anisotropy (SKS, SKKS and sSKS) and green for phases that have similar arrival times. It is obvious that there is no major wave interference between different phases as the SKS-SKKS pairs have different arrivals that are well separated in time for the whole distance range. Colored circles display the characteristics for the SKS-SKKS pairs in the corresponding seismograms (null-split, split-null, null-null, split-split). On the right the geological units (Gaál & Gorbatschev, 1987; Gorbatchev, 2004) are shown at which the corresponding stations are sited. It is obvious that discrepant pairs are recorded across different units from southwestern Sweden (Sveconorwegian domain) up to northern Finland (Paleoproterozoic domain). As seen in more detail in Fig. DR4 for SKS and sSKS the same pattern is observed. A map view of the stations and raypaths is shown in Figure DR11.

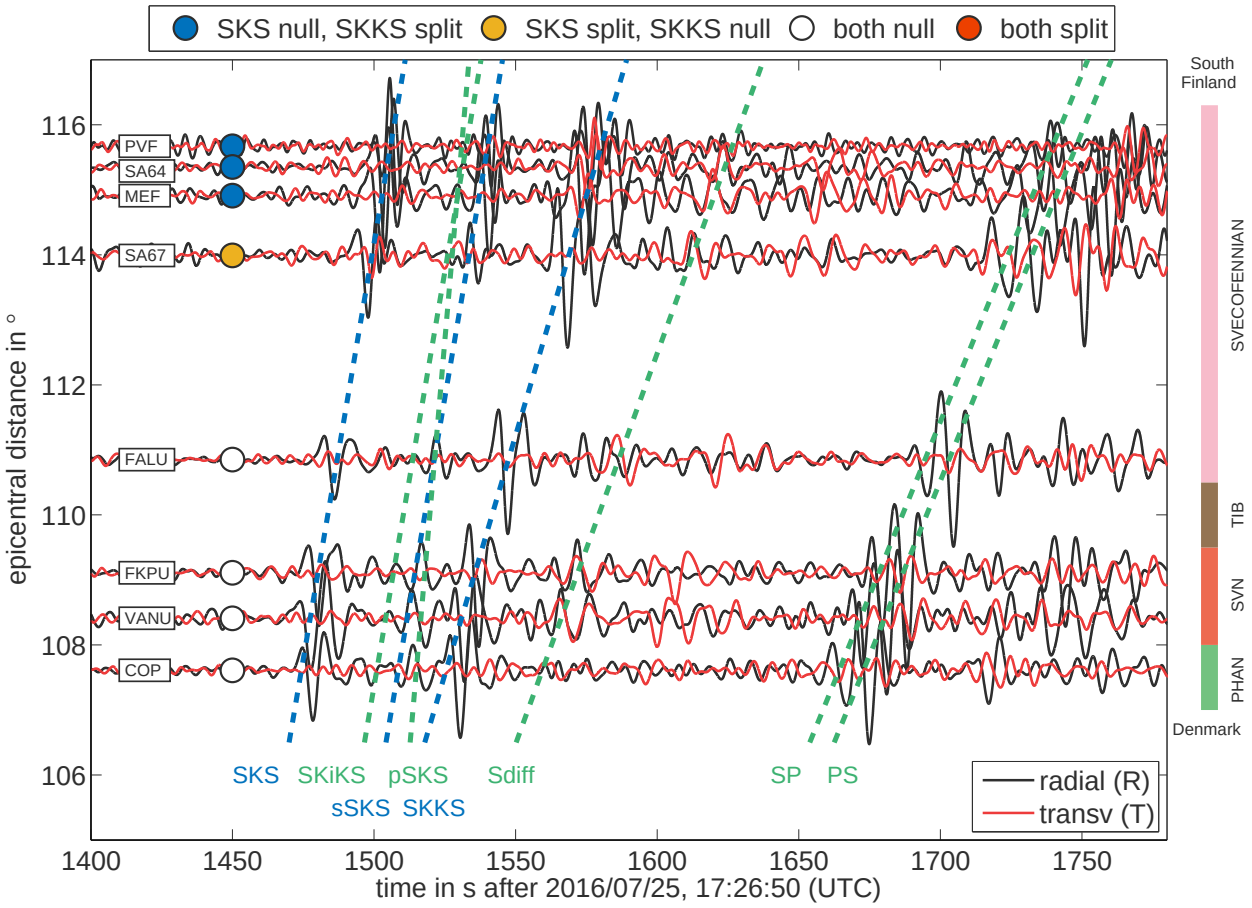

Figure DR8: Record section with seismograms of the radial (black) and transverse (red) components of a Chile event on 2016/07/25. Theoretical arrivals of different phases based on the iasp91 earth model (Kennett, 1991) are shown as dashed lines. Blue indicates phases that were used in this study to probe lowermost mantle anisotropy (SKS, SKKS and sSKS) and green for phases that have similar arrival times. It is obvious that there is no major wave interference expected for the SKS-SKKS pairs since the different arrivals are well separated for the whole distance range. Colored circles display the characteristics for the SKS-SKKS pairs in the corresponding seismograms (null-split, split-null, null-null, split-split). On the right the geological units (Gaál & Gorbatschev, 1987; Gorbatchev, 2004) are shown at which the corresponding stations are located. A map view of the stations and raypaths is shown in Figure DR11.

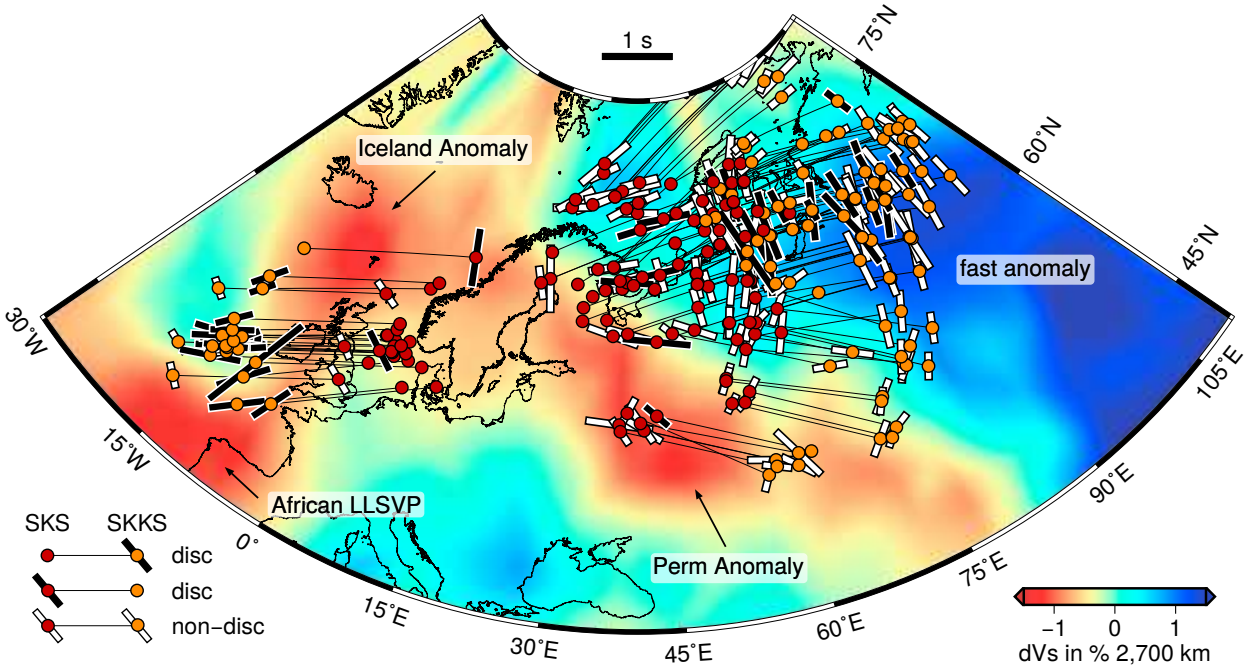

Figure DR9: SKS-SKKS pierce points at 2,700 km depth, calculated with the tauP toolkit (Crotwell et al., 1999) and the iasp91 earth model (Kennett, 1991), atop of the GyPSuM model (Simmons et al., 2010) in the lower mantle. Pairs are marked with red (SKS) and orange (SKKS) dots. For discrepant pairs the split phase is indicated with a white bordered black bar oriented in the direction of the fast axis ϕ. Non-discrpeant pairs (only split-split) are marked with a black bordered white bar at the SKS and SKKS pierce points (also oriented in the direction of the fast axis ϕ).

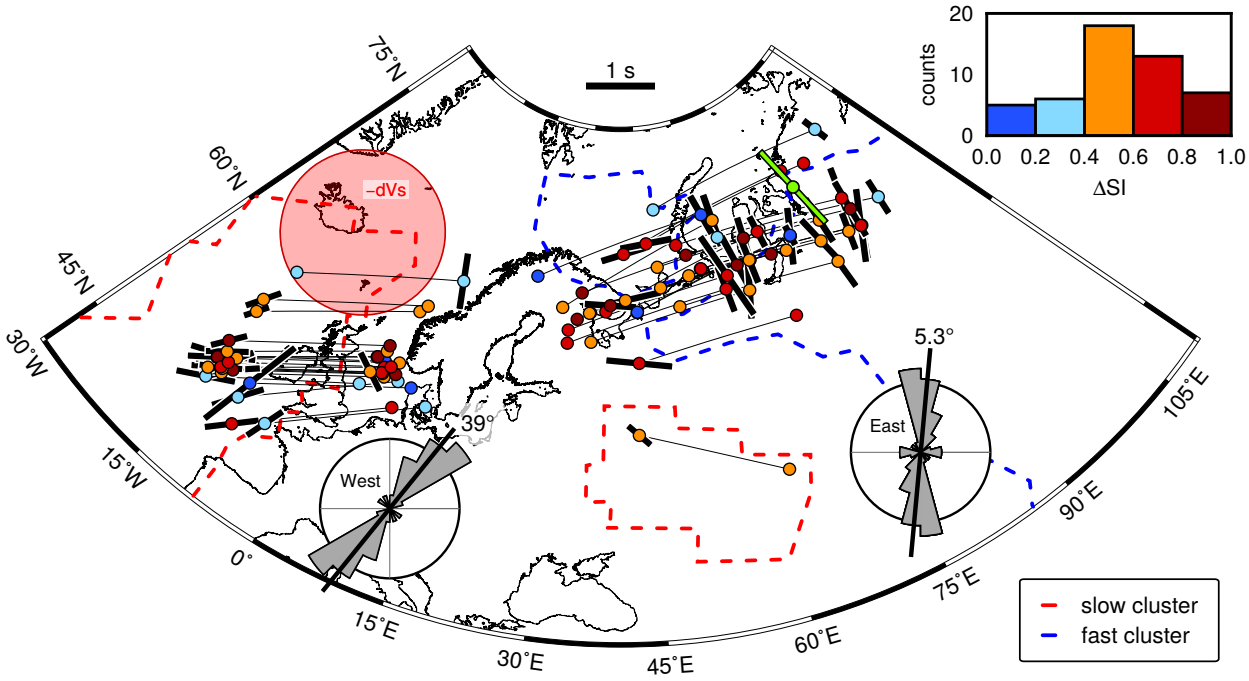

Figure DR10: D" pierce points of the discrepant SKS-SKKS pairs along with the measured ΔSI values (filling of dots). The histogram highlights the number of observations binned in steps of 0.2. Rose plots indicate the distribution of ϕ for the split phases, separated into western and eastern cluster. The averages of the split SKKS phases for east and west are shown as black bars with ϕ_{mean} = 5.3° (east) and ϕ_{mean} = 39° (west) The green bar displays observed ScS splitting after Wookey & Kendall (2008). Red and blue dotted lines encompass regions of model agreement regarding slow (Lekic et al., 2012, see also Fig. DR13) and fast v_S (Shepard et al., 2017, see also Fig. DR12). The dimension of the indicated slow-v_S zone beneath Iceland (He et al., 2015) is shown as red circle.

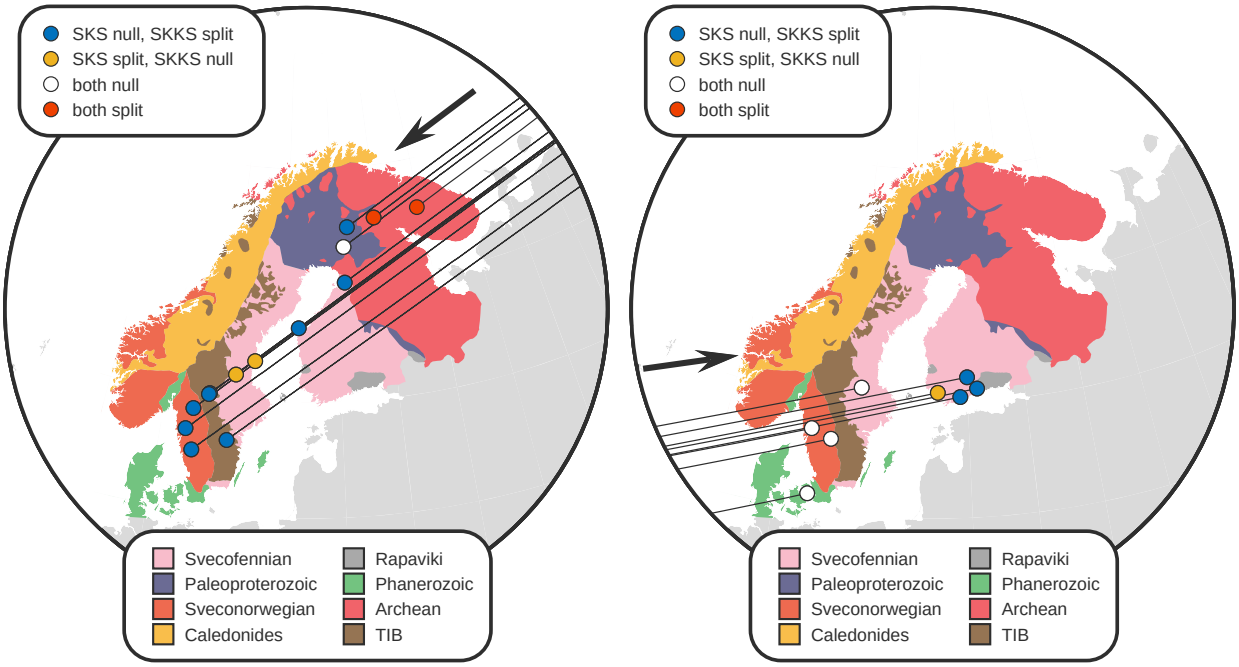

Figure DR11: Locations of recording stations shown in Figures DR7 and DR8 atop the simplified geological units of Fennoscandia after Gaál & Gorbatschev (1987); Gorbatchev (2004). The raypaths (thin black lines) for the events below Papua New Guinea on 2016/08/31 (left) and Chile on 2016/07/25 (right) as well as the directions of the arriving wavefronts (black arrows) are shown.

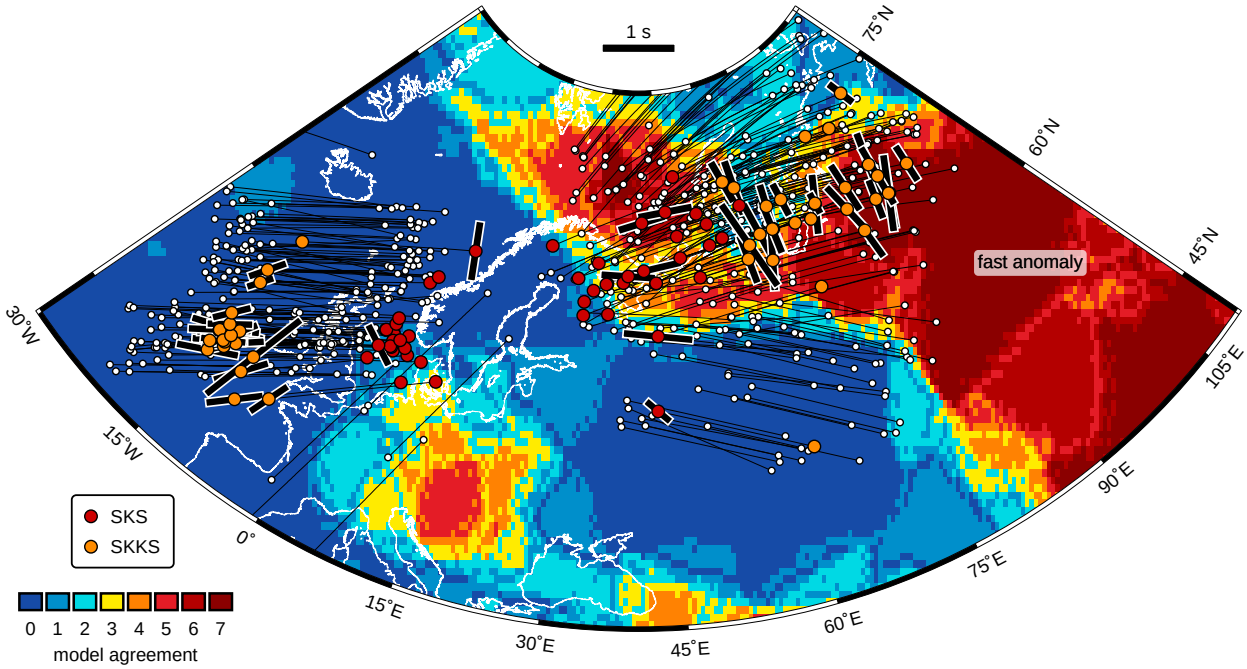

Figure DR12: SKS-SKKS pierce points at 2,700 km depth, calculated with the tauP toolkit (Crotwell et al., 1999) and the iasp91 earth model (Kennett, 1991), atop of the vote map analysis of Shepard et al. (2017). Discrepant pairs are marked with red (SKS) and orange (SKKS) dots, the split phase is indicated with a white bordered black bar oriented in the direction of the fast axis ϕ and scaled by the delay time δt (as observed at the station). Related pierce points are connected by thin black lines. White dots indicate non-discrepant pairs (either both are split or both are null). This figure implies that anisotropy in the lowermost mantle beneath northwestern Siberia is located along the edges of a fast anomaly that is observed in all seven tomography models.

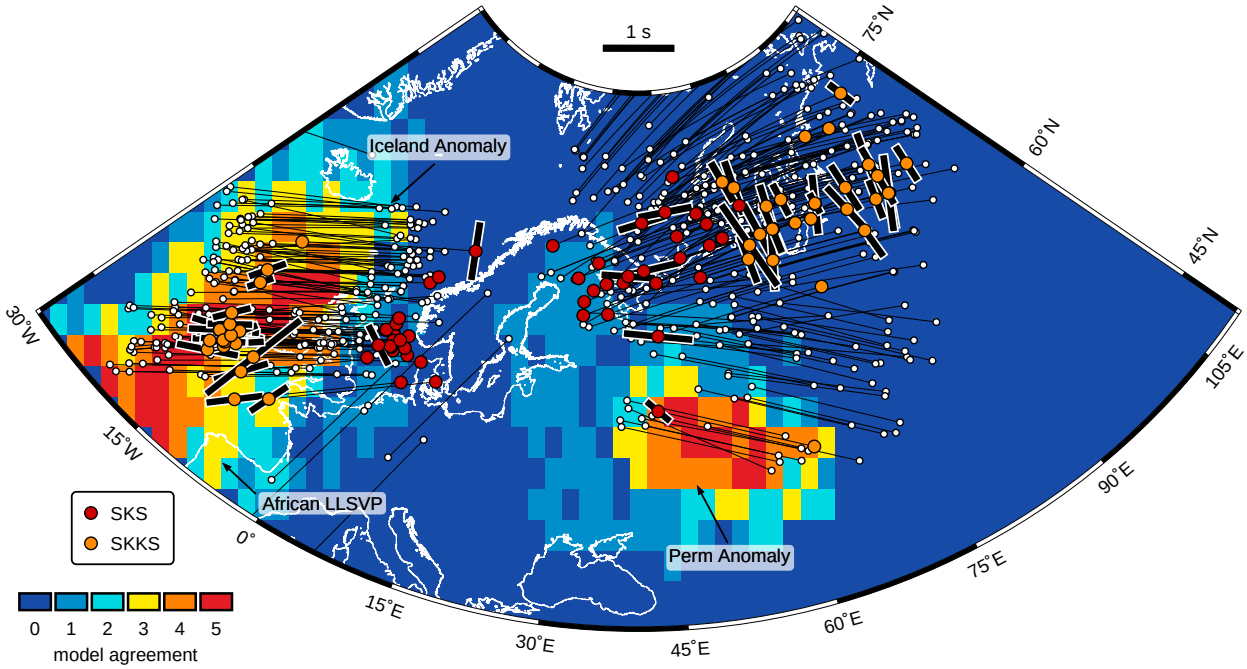

Figure DR13: SKS-SKKS pierce points at 2,700 km depth, calculated with the tauP toolkit (Crotwell et al., 1999) and the iasp91 earth model (Kennett, 1991), atop of the cluster analysis of Lekic et al. (2012) in the lower mantle. Discrepant pairs are marked with red (SKS) and orange (SKKS) dots, the split phase is indicated with a white bordered black bar oriented in the direction of the fast axis ϕ and scaled by the delay time δt (as observed at the station). Related pierce points are connected by thin black lines. White dots indicate non-discrepant pairs (either both are split or both are null). This figure implies that anisotropy in the lowermost mantle is located along the edges of a connection between the northern extension of the African LLSVP and a slow velocity anomaly below Iceland.

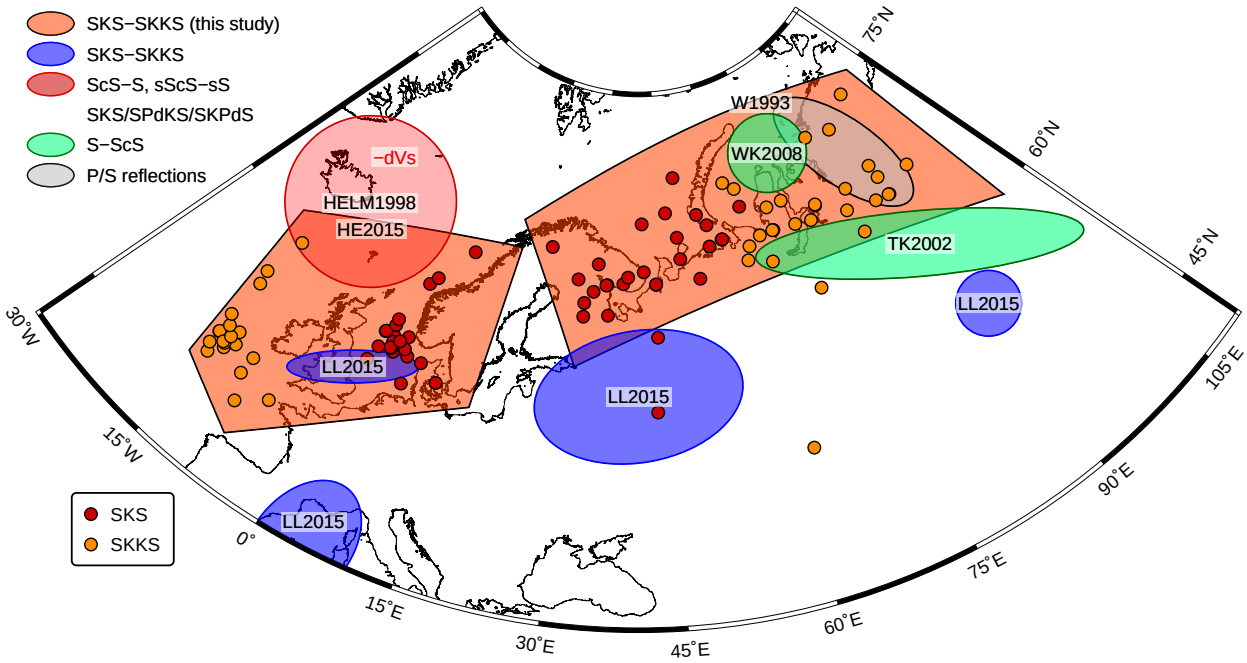

Figure DR14: Overview about areas in which anomalous lowermost mantle structure was observed based on different seismic phase types. The two large patches colored in orange encompass the regions identified in this study based on SKS-SKKS splitting discrepancies. Red and orange circles indicate the SKS-SKKS pierce points at 2,700 km depth, calculated with the tauP toolkit (Crotwell et al., 1999) and the iasp91 earth model (Kennett, 1991). Blue areas show regions of discrepant SKS-SKKS observations that were attributed to lowermost mantle anisotropy after a correction for (known) shallower anisotropy (LL2015, Long & Lynner, 2015). The red circle shows the estimated dimension of the indicated slow shear velocity zone beneath Iceland based on SKS/SPdKS/SKPdS waveform interference analysis (HELM1998, Helmberger et al., 1998) and ScS-S and sScS-sS differential traveltime residuals (HE2015, He et al., 2015). Green patches indicate areas where ScS-S splitting was used to constrain D" anisotropy that was associated with paleo-subduction (TK2002, WK2008, Thomas & Kendall, 2002; Wookey & Kendall, 2008). An area of anomalous P- and S-wave reflections at the D" is shown as gray ellipse (W1993, Weber, 1993)